

Numerical characterization of downburst wind field at WindEEE dome

Ibrahim Ibrahim^{1,2}, Haitham Aboshosha³ and Ashraf El Damatty^{*1,2}

¹Department of Civil and Environmental Engineering, Western University, London, Ontario, Canada

²The Wind Engineering, Energy and Environment (WindEEE) Research Institute, Western University, London, Ontario, Canada

³Department of Civil Engineering, Ryerson University, Toronto, Ontario, Canada

(Received August 28, 2018, Revised December 9, 2019, Accepted December 22, 2019)

Abstract. Downbursts are acknowledged for being a major loading hazard for horizontally-extending structures like transmission line systems. With these structures being inherently flexible, it is important to characterize the turbulence associated with the wind flow of downburst events being essential to quantify dynamic excitations on structures. Accordingly, the current study numerically characterizes the downburst wind field of open terrain simulated at the Wind Engineering, Energy and Environment (WindEEE) dome testing facility at The University of Western Ontario in Canada through a high-resolution large eddy simulation (LES). The study validates the numerical simulation considering both the mean and the turbulent components of the flow. It then provides a detailed visual description of the flow at WindEEE through the capabilities enabled by LES to identify the key factors affecting the flow. The study also presents the spatial distribution of turbulence intensities and length scales computed from the numerical model and compares them with previous values reported in the literature. The comparison shows the ability of the downburst simulated at WindEEE to reproduce turbulence characteristics similar to those reported from field measurements. The study also indicates that downburst turbulence is well-correlated circumferentially which imposes high correlated loads on horizontally-distributed structures such as transmission lines.

Keywords: downburst; WindEEE; Large Eddy Simulation (LES); turbulence; length scales; high intensity wind

1. Introduction

Over the past decades, experimental wind tunnel testing focused on the simulation of Atmospheric Boundary Layer (ABL) and its effect on various structures. Recently, this has extended to include the simulation of High Intensity Wind (HIW) events associated with thunderstorms and represented by downbursts and tornadoes due to their significance in Wind Engineering applications. Li (2000) reported that strong thunderstorms including downbursts and tornadoes are responsible for 90% of the weather-related failures of transmission line structures in Australia. Dempsey and White (1996) also reported that 80% of weather-related failures of transmission lines are attributed to high intensity wind, which incorporates tornadoes and downbursts.

A downburst is known as an intense downdraft that impinges towards the ground and convects radially causing high damaging wind speeds near the ground as described by Fujita (1985). This can be viewed as the opposite of the tornado, where a warm updraft of swirling air forms that sucks the air near the ground and feeds into the cloud base. Despite the fact that downbursts have relatively lower wind speeds than tornadoes, they impose greater damage to structures because of their higher occurrence rate. Detection of downbursts is very challenging compared with synoptic winds. That is because downbursts have relatively short durations (i.e., 20-30 min) and have relatively small size (up

to 5000 m) as reported by Hjelmfelt (1988). This complexity encouraged many researchers to study downbursts experimentally and computationally in addition to the full-scale measurements.

Earlier research was directed to full-scale measurements trying to provide field data for the newly explored wind event. Meteorological projects like the Northern Illinois Meteorological Research on Downbursts (NIMROD) and the Joint Airport Weather Studies (JAWS) were reported by Fujita (1985), while the Federal Aviation Administration Lincoln Laboratory Operational Weather Studies (FLOWS) project has been reported by Wolfson *et al.* (1985). More recent field measurements have been reported by Orwig and Schroeder (2007) who presented the results obtained from a linear array of mobile towers for two captured events. They also presented their analyses for the results that were compared to synoptic wind data analysis. Choi (2004) has also reported measurements taken using one tower for more than 50 thunderstorm events. The author furtherly investigated the different variables affecting the velocity profiles of the measured events. In addition, a relatively large project, that took place between 2009 and 2012, has been reported by Solari *et al.* (2015a) as an extensive in-situ wind monitoring network. The Wind and Ports project relies on 22 ultrasonic anemometers to capture high-resolution thunderstorm records that are then processed to extract statistical properties of thunderstorm events. Gunter and Schroeder (2015) have also presented measurements collected using two mobile Doppler radars to provide an enhanced understanding of the vertical profiles through analyzing three events.

*Corresponding author, Professor
E-mail: damatty@uwo.ca

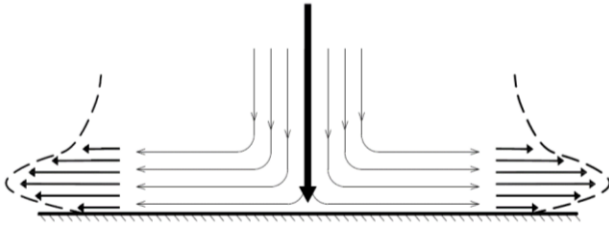


Fig. 1 Schematic view of the impinging jet model

Adjacently, researchers have managed to replicate the phenomenon of downburst experimentally at laboratory scales. This was mainly done through the impinging jet model as suggested by Hjelmfelt (1988) to resemble much of the flow characteristics of microbursts. This was further studied by researchers like Wood *et al.* (2001), Chay and Letchford (2002), Mason *et al.* (2005), Sengupta and Sarkar (2008), McConville *et al.* (2009), Das *et al.* (2011) and Li and Ou (2012). All the previously mentioned attempts were executed in relatively small laboratory scales. While these efforts are credited for providing much of our current understanding of downbursts, their small scales did not allow for a detailed understanding of the flow field including the turbulence structures.

This has motivated the researchers at University of Western Ontario to build the Wind Engineering, Energy and Environment (WindEEE) dome, a unique facility that can simulate downbursts at unprecedented scales.

Furthermore, a wider spectrum of researchers has simulated the downburst numerically utilizing computational fluid dynamics (CFD) through different schemes for physical models. Choosing between cloud models, cooling source models and impinging jet models, researchers usually balanced the accuracy of the results provided with the computational power needed. For example, researchers with interest in wind engineering usually preferred the sub-cloud model over the full cloud model due to its computational efficiency, as well as its ability to resolve near the surface flows (Mason *et al.* 2009). Examples for the cloud scheme of downburst simulation could be found through the work of researchers like Lin *et al.* (2007), Mason *et al.* (2009), Mason *et al.* (2010), Otsuka (2006) and Vermeire *et al.* (2011). As for the impinging jet scheme, illustrated in Fig. 1, researchers like Wood *et al.* (2001), Chay and Letchford (2002) and Sengupta and Sarkar (2008) have used the scheme, looking at the wind field at the steady state (i.e., after the downdraft hit the ground) and achieved comparable results. Other researchers like Mason *et al.* (2005), Kim and Hangan (2007), Xu and Hangan (2008), and Aboshosha *et al.* (2015) investigated the transient nature of the downburst wind field before and after the downdraft hits the ground.

Researchers in the numerical stream have used several viscous models, from RANS and its several derived models ($k-\epsilon$, RSM and $k-\Omega$), to the shear adaptive simulation (SAS), shear stress transport (SST), and finally the large eddy simulation (LES) model. Out of the researchers who studied the turbulent component of the flow, those who utilized the LES model including Hadziabdić (2006), Chay

et al. (2006), Sengupta *et al.* (2008) and Aboshosha *et al.* (2015) showed the adequacy of using the LES model in resolving downburst flows. Yet, for resolving the turbulent component, Tamura and Kareem (2013) state that the scales of turbulence resolved are bounded at a maximum that is attributed to the domain size, and a minimum attributed to the grid resolution. This implies that for turbulence to be resolved, the grid resolution, through the flow path, shall be kept constant and at least smaller than or equal to the minimum turbulence scale required to be resolved, similar to what Elshaer *et al.* (2016) have applied. The aforementioned feature, although deterministic for the resolved turbulence scales, was not taken into consideration by previous studies. The general approach was to densify the grid near the ground where flow features are of most importance, and coarsen it elsewhere for computational efficiency. This leads to the scales being dictated by larger grid sizes, which impacts the range of captured turbulence frequencies. A more detailed collection of these efforts associated with downburst flow studies can be found through the comprehensive review done by Aboshosha *et al.* (2016).

The current study belongs to the numerical simulation group but focuses on replicating the downbursts simulated experimentally at the WindEEE dome. The study aims at characterizing the detailed turbulent wind field generated at WindEEE and understanding the role of the experimental elements affecting the flow. The study utilizes the wind field collected from a previous downburst experiment reported by Elawady *et al.* (2016) and Elawady *et al.* (2017) to validate the CFD model. The manuscript is presented in five sections. In section 1 (this section), an introduction and a literature review are presented. Section 2 illustrates the previous experiment conducted at WindEEE. Section 3 discusses the detailed CFD simulations of the WindEEE dome and Section 4 presents the results from the simulations. Finally, section 5 includes the conclusions and recommendations.

2. Experimental simulation

The experiment presented in this section was part of the work conducted by Elawady *et al.* (2017) as a preliminary stage of the aeroelastic transmission line model testing presented in their study. The procedures described hereafter were aiming at characterizing downburst wind field at the WindEEE dome, before testing the aeroelastic model. The WindEEE dome, schematically shown in Fig. 2, utilizes 106 individually controlled fans to simulate a variety of straight flows, as well as axisymmetric flows like tornadoes and downbursts. Similar to conventional wind tunnel methods, the turbulent component can be imposed using upstream flow modifiers and about 1600 roughness blocks. The blocks are grouped into a number of sectors and each sector can be individually controlled to reach a height between 0 and 12 inches to simulate target terrain exposure for a wide range of length scales. Simulation of the downburst is performed by pressurizing the air in an upper room (called the upper plenum) using a number of 6 fans, and then opening the vents between the upper room and the space

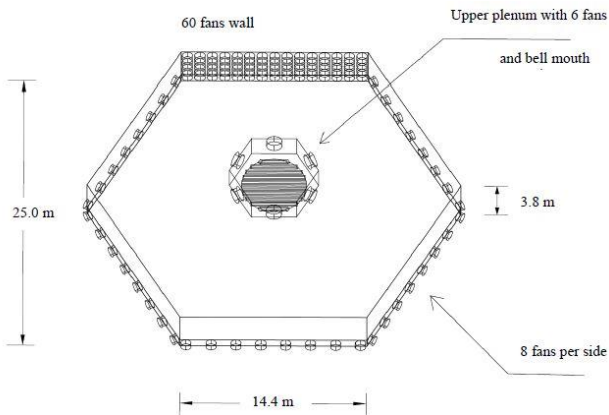


Fig. 2 Schematic view of the WindEEE dome as per (Jubayer *et al.* 2016)

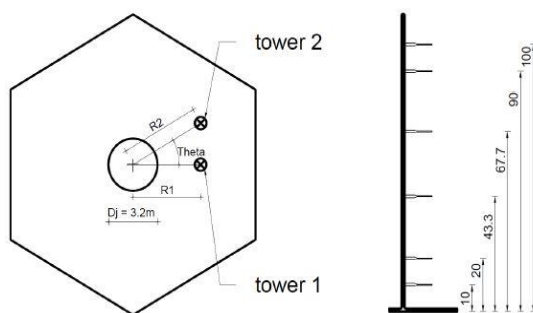


Fig. 3 Probe tower locations and probe heights in centimeters

underneath to form the downdraft. The vents connecting the room to the space underneath operate in a circular nozzle (called the bell mouth) as shown in Fig. 2. The bell mouth allows for simulating downbursts with variable jet diameters (here it was set to 3.2 m) and it has a height of 3.8 m from the ground. Although this leads to relatively small height-to-diameter ratio of 1.2, such a small ratio was proven adequate for producing reliable downburst wind field (Aboshosha *et al.* 2015 and Elawady *et al.* 2017). After impingement, the flow convects radially until it reaches the lower peripheral, which act as outlets by opening the louvers without the fans being operated. The downdraft speed depends on the power input to pressurizing air in the upper plenum and it was estimated to be between 4-9 m/s for the utilized fan power.

A basic wind field was collected experimentally using 12 high-resolution cobra probes distributed evenly on 2 towers as shown in Fig. 3 and operating at a sampling frequency of 156 Hz. These probes were oriented towards the chamber's centre to align the downburst radial velocity component with the longitudinal component of the probes. Since the flow field was characterized by only 2 towers, multiple downburst tests were conducted while altering the tower locations. The location of the first tower is referred to as **R1** and the second tower location is referred to as **R2** as shown in Fig. 3. The first tower was consistently placed at the location of the maximum radial speed which was found to be at $R1=1.0 D_j$. The second tower was placed at a variable distance **R2** ranging between $0.7 D_j$ and $3.0 D_j$ and

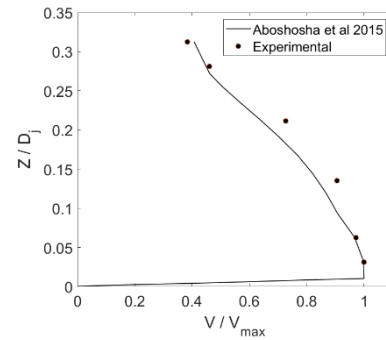


Fig. 4 Radial velocity profiles comparison

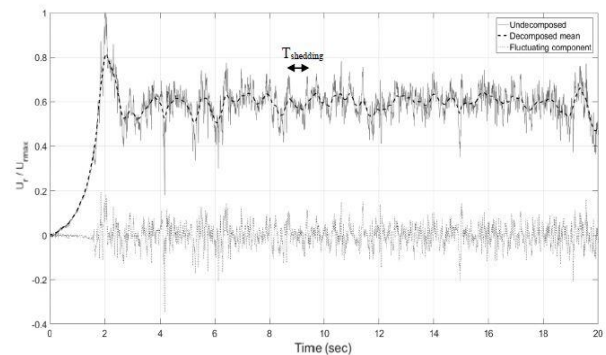


Fig. 5 Decomposed time history

at an angle theta ranging between -60 to +60 degrees. The measurements were retaken to assess the repetitiveness of the profiles corresponding to certain fan power and it was found satisfactory.

Open terrain exposure was simulated by setting the roughness blocks at 6 inches. The profile of the mean radial velocities resulting from the chosen block height was compared with that simulated by Aboshosha *et al.* (2015) for open exposure and have shown a good agreement as indicated in Fig. 4.

Highlighting the comparison discussed above, the mean component was extracted from the time histories using a decomposition technique similar to that reported by Holmes *et al.* (2008). The decomposition technique relies on the shedding frequency, where the cut-off frequency, separating the mean and the fluctuating component, is taken as a multiple of the shedding frequency. The shedding frequency is that of the main vortices near the ground as described by Kim and Hangan (2007). This technique will be discussed in more details in the following section. Fig. 5 shows the decomposed time history acquired using the mentioned technique.

3. Numerical model setup

Computational Fluid Dynamic (CFD) simulations replicating the downbursts simulated at the WindEEE dome are discussed in this section. First, details about the governing equations and CFD solver are provided. This is followed by a description of the employed model, boundary conditions and details of the simulation are presented.

3.1 LES governing equations

CFD models were conducted using Large Eddy Simulation (LES) due to its efficacy to properly simulate the turbulent component and thus the transient details of the flow field. Navier-Stokes Equations presented by equations (1~5) are resolved at each time step using ANSYS FLUENT solver (ANSYS Inc. 2016)) employing the dynamic sub-grid model introduced by Germano *et al.* (1991) and then modified by Lilly (1992). In this model, the model constant C_s in Eq. (5) is computed dynamically based on the resolved flow field and has proven to properly simulate the turbulence energy dissipation. Pressure and velocity coupling was conducted using Pressure-Implicit with Splitting of Operators (PISO) scheme. This scheme has proven to outperform for cells with relatively high skewness. This usually proves worthy, although the computing time per iteration might increase compared to the other coupling schemes. As for the spatial discretization, the Least Squares Cell-Based, Second Order and Bounded Central Differencing schemes are used for gradient, pressure and momentum discretization respectively. Finally, for the temporal discretization, second-order implicit time integration was chosen. These choices were based on the recommendations and descriptions of all available schemes in the program's documentation (ANSYS Inc. 2016).

$$\frac{\partial \bar{u}_i}{\partial t} + \bar{u}_j \frac{\partial \bar{u}_i}{\partial \bar{x}_j} = -\frac{1}{\rho} \frac{\partial \bar{P}}{\partial \bar{x}_i} + \frac{\partial}{\partial \bar{x}_j} (-\tau_{ij} + 2\nu \bar{S}_{ij}) \quad (1)$$

$$\tau_{ij} = \bar{u}_i \bar{u}_j - \overline{u_i u_j} \quad (2)$$

$$\bar{S}_{ij} = \frac{1}{2} \left(\frac{\partial \bar{u}_i}{\partial \bar{x}_j} + \frac{\partial \bar{u}_j}{\partial \bar{x}_i} \right) \quad (3)$$

$$\tau_{ij} - \frac{1}{3} \delta_{ij} \tau_{kk} = -2\nu_e \bar{S}_{ij} \quad (4)$$

$$\nu_e = (C_s \Delta)^2 |\bar{D}| \quad (5)$$

where \mathbf{u} , \mathbf{t} , ρ , \mathbf{P} , $\boldsymbol{\tau}$, ν and \mathbf{S} stand for velocity, time, density, pressure, subgrid-scale turbulent stresses, molecular viscosity coefficient and the strain rate tensor. The i , j and k annotations represent the along, across and out-of-plane directions. ν_e is the eddy viscosity, $|\bar{D}|$ is the grid scale tensor, Δ is the cell size and C_s is the Smagorinsky constant.

3.2 Model details

The computational domain was carefully constructed to include most of the elements utilized in the experimental setup as shown in Fig. 2. This includes detailed modeling of the inflow condition (i.e. the bell mouth with the opening flaps, roughness blocks and the outflow condition). As shown in Fig. 6, the bell mouth was fully modelled with its flaps (vents). The plenum, on the other hand, was spared, where a constant velocity (4 m/s) with synthesized turbulence inlet boundary condition with the jet diameter shall suffice to resemble its physical role. Turbulence intensity of the downdraft was unknown during the test

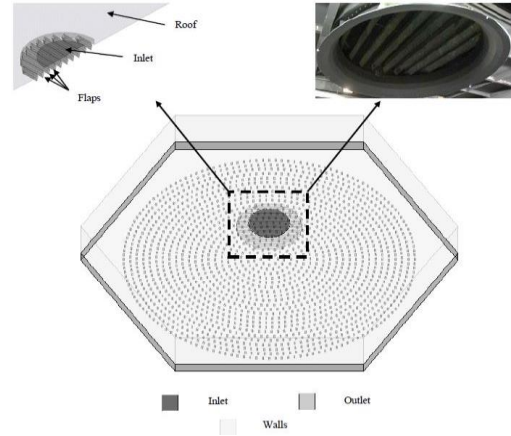


Fig. 6 Boundary conditions assignment for different boundaries with details of inlet

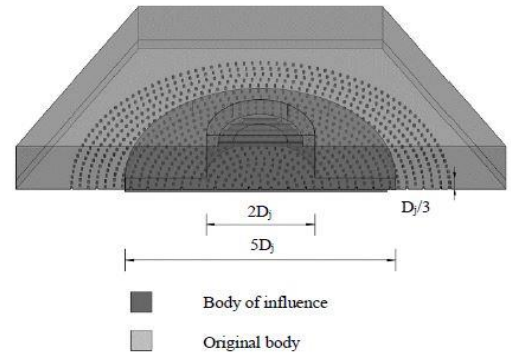


Fig. 7 Influence zone

since there was no cobra probe placed in the test near the bell mouth. To account for this in the simulation, three downdraft turbulent intensities of 0%, 7% and 15% were considered and the simulation was repeated for each. It was found that the results for the 15% turbulence intensity led to the best match with the experiment as will be discussed later in the following section. The roughness blocks were simulated exactly as they were considered during the test. A number of 1600 blocks was used with a block dimension of 4 x 4 inches (~10 cm x 10 cm) by 6" (15 cm) for open exposure as verified by Elawady *et al.* (2017) by comparing the resulting profile with previous profiles from the literature. As for the outlet, the geometric projection of the peripheral was modelled as a continuous surface throughout the perimeter, where the louvers of the fans were not modelled due to their insignificance on the flow features.

After constructing the model, ANSYS Mesher package was utilized to produce a volumetric grid to resolve the flow. The mesh density distribution was chosen such that the volume where the main flow develops shall have consistent grid size. Fig. 7 shows the volumetric section where the influence zone was chosen. As demonstrated, the zone was chosen to bound the core of the flow at a diameter of twice the jet diameter descending from the inlet. Stretching beyond the jet diameter was decided to make sure the development of vortices due to Kelvin-Helmholtz instability is fully captured within the fine grid range. In

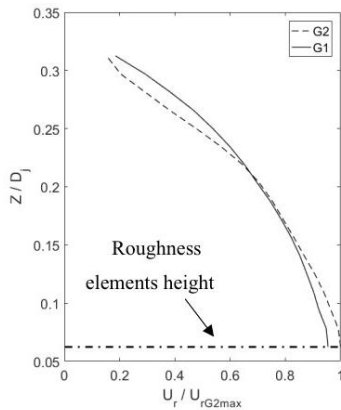


Fig. 8 Grid dependency plot

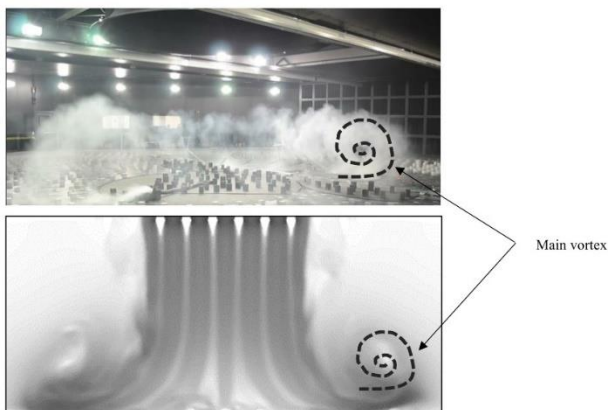


Fig. 9 Experimental smoke visualization vs CFD velocity contour

addition, the lower segment of the domain, where the convective flow is expected to occur, was also included in the fine grid zone. This zone was truncated at a radial distance of 2.5 times the jet diameter for computational efficiency.

Choosing polyhedral cells due to their efficiency in resolving rotational flows (ANSYS Inc. 2016), a total cell count of ~ 5 million (G1) for a cell size of $D_j/64$, and ~ 9 million (G2) for a cell size of $D_j/80$ were obtained. A limited grid independence test was carried out for the two grids based on the profiles of the mean radial velocities at the instant and position of maximum velocity. The radial velocity was chosen to be the main focus of this study due to its significance on the loading of structures (Elawady and El Damatty (2016)). The resulting profiles from both grids are shown in Fig. 8, which demonstrates that both grids lead to compatible profiles. It should be noted that the region beneath the dashed line in the figure has been excluded from the plot, as it resembles the height that would be affected by the roughness elements. The maximum difference between the two profiles was found less than 5% at the region where the peak velocities are expected to develop, which indicates the grid independency of the results. It is worth to note that the coarser grid (i.e., 5 million cells) was utilized in presenting the results on the following sections. Fig. 9 shows a comparison between the CFD velocity contours and the experimental smoke

visualization, showing the relevance of the developed main vortex in both simulations.

With the aforementioned configuration, the computational cost to run each simulation for 15 seconds ($1e-3$ second time step) after initialization was around 5000 core hours. Using 2 computing nodes, 16 core each, with 4 GB of dedicated RAM for each core, the simulation would run for around 6 days.

4. Results

The CFD model described in the previous section was utilized to obtain the wind field for the downburst simulation and the resulting wind field is discussed in this section. First, an overview of the transient nature of the wind field is presented, which is then followed by describing the utilized technique to decompose the wind field into a non-stationary “running” mean component and a turbulent component. Afterwards, a comparison between mean and turbulent components of the wind field obtained from the CFD simulations with those obtained from the experiment is provided for validation before presenting spatial representations of turbulence properties obtained from the CFD simulation.

4.1 Development of wind field

Snapshots of the velocity contours of different time instants showing how the wind field gradually develops through the domain can be seen in Fig. 10. The instantaneous shots are presented at a plane P1, which is a vertical plane passing through the center of the jet and orthogonal to the louvers. The snapshots are calibrated in τ , which is the time normalized by the peak radial velocity instant (T/T_{max}). At the beginning of the simulation, when the flow is released from the inlet boundary, the presence of the flaps with their considerable cross-section generally impacts the flow. This can be deduced throughout the whole time range, where the flaps cause streaming of the flow within the region of pre-impingement. The streaming limits the contribution of the inner region of the descending downdraft to the interaction between the downdraft and the ambient air. Such interaction can be seen in the first three time instances (i.e., $\tau = 0.2, 0.4$ and 0.6) where the Kelvin-Helmholtz instability is formed as a result of the shear between the descending and the still air. After that, time instances beyond the impingement ($\tau > 0.8$), illustrate the radial convection mechanism, where the transported vortices are obstructed by the roughness elements. The influence of the modelled elements can be generally described as turbulence generators for the convecting flow. Yet, some important features can be noticed from the figure. Firstly, the roughness elements right below the centre of the jet can be clearly seen to entrap flow structures ($\tau > 0.6$). The fact that the dimensions of the modelled elements result in significant canopy zones can also be noted from the displayed figure. Adding to the streaming caused by the flaps, this is believed to result in preventing the inner core of the jet from contributing to the radial out

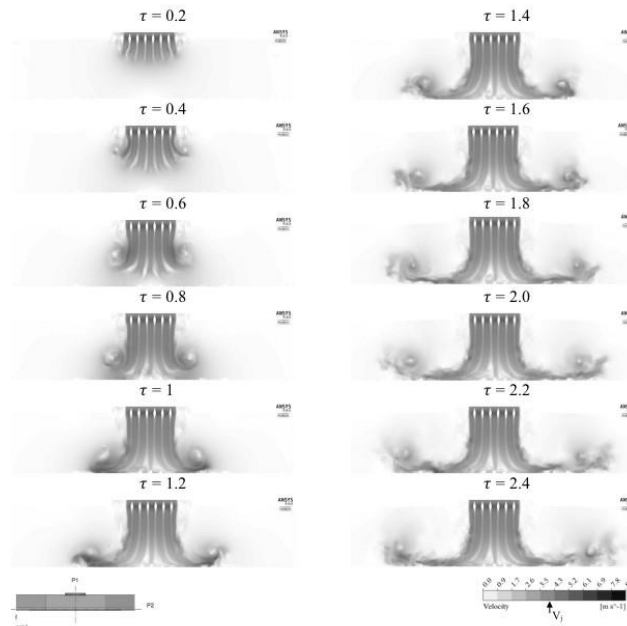


Fig. 10 Development of wind field represented by velocity contours for different $\tau = t / T_{max}$ at P1

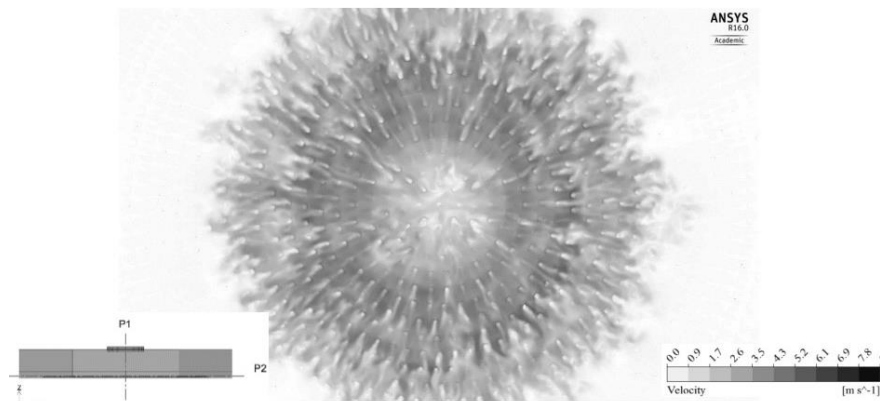


Fig. 11 Roughness blocks impact on the flow through velocity contour of horizontal plane at $Z=0.05 D_j$ at P2

flow after impingement. This means that the main driving force of the outflow is generated by the outermost part of the jet. Secondly, the main convecting vortex generally maintains its structure throughout the monitored period, surpassing the main areas of interest located at a jet diameter distance from the jet centre. The secondary vortex formed after impingement due to separation, that was reported by Kim and Hangan (2007) and Aboshosha *et al.* (2015) and can be seen to form the snapshot at $\tau=1$. However, the following instances show that the newly formed structure fails to keep up with the flow and diminishes as it encounters more roughness blocks. This can be again attributed to the size of the roughness elements, as well as the spacing between them which is comparable to that of the formed vortices, leading to destroying the structure of the secondary vortex. Accordingly, only the main vortex is able to maintain its structure and carry the driving energy for the radial convection. Thirdly, closely observing the development of the flow, secondary vortices formed due to quasi-static

Kelvin-Helmholtz instability reported by Kim and Hangan (2007) can be noticed. These are the structures that follow the main vortex from the inlet, later as the flow progresses. Finally, while the impact of the flaps is clearly observable in Fig. 10, the roughness blocks also have a noticeable effect that can hardly be seen from the elevation view. Fig. 11 representing a planar view at P2, which is a horizontal plane at an elevation right above the blocks height clearly demonstrates the effect they have on the flow. The unevenly distributed shades are revealing the shielding, channeling and irregularity the blocks impose on the flow. Noting that the block height is in the order of 5 percent of the jet diameter for the open exposure, the canopy zone over shades the zone where peak radial velocities are expected.

4.2 Wind field decomposition

The wind field associated with downburst events is uniquely distinguished by its non-stationarity which sets it apart from the conventional atmospheric boundary layer

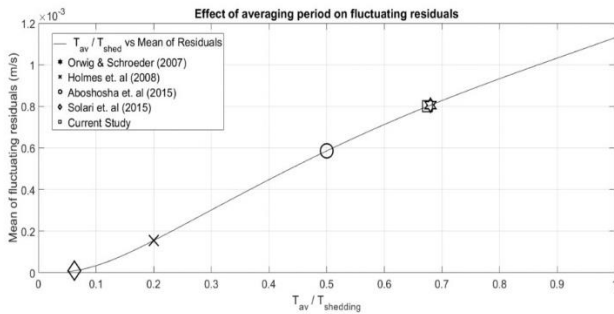


Fig. 12 Effect of averaging period on mean of fluctuating residuals

(ABL) flow. While ABL is characterized by a constant mean and a zero average fluctuating component, the downburst has a mean value that varies with time, and a residual component that can be extracted by subtracting the mean from the flow. This is widely agreed upon in literature, where researchers like Holmes *et al.* (2008), Aboshosha *et al.* (2015a) and Solari *et al.* (2015b) used a moving average technique to discretize the mean component from the time history. The technique relies on an averaging window by which the time history is averaged within the range of this moving average, resulting in a slowly varying mean, while the residual is considered to be the zero average fluctuating component. The challenge here is to decide upon the value of this moving average window. The chosen value shall result in a mean component that resembles the main driving flow characteristics, without a significant fluctuating component. Researchers like Holmes *et al.* (2008) and Solari *et al.* (2015a) have tried different values of averaging periods, and relied on their judgement to decide on which period could result in mean and fluctuating components that satisfy the above criteria. Yet, researchers like Aboshosha *et al.* (2015a) relied on equation (6) to calculate the averaging period T_{av} as being a factor X_{av} , taken to be 0.67 in this study, multiplied by the shedding period $T_{shedding}$, which is in the order of 1 second, being the period at which the vortices shed post the ramp up as shown in Fig. 5. This technique with an averaging period less than the shedding vortex assures that the main vortex is included in the running mean. Furthermore, the value of 0.67 is chosen to ensure the applicability to structural applications, where frequencies of structures such as transmission line systems are within the fluctuating component's frequencies. This method was utilized in the current study to decompose running mean which was subtracted from the overall wind field to obtain the turbulent component. Fig. 12 illustrates the effect the factor X_{av} has on the mean value of the fluctuating component, which is expected to have a near zero value for a representative fluctuating component. As shown, different studies in the literature chose values generally smaller than unity. Although the current study seems to yield a higher mean of the residuals, the chosen value of 0.67 still yielded comparable results, where the mean of the fluctuating residuals is considerably small. Furthermore, the chosen value is shown to maintain the mean characteristics as indicated by Holmes *et al.* (2008) and Solari *et al.* (2015a),

where the mean profile follows the general characteristics of the flow as shown in Fig. 13 described below. The calculated averaging period is then applied to the velocity time history using a bi-directional moving average filter to eliminate the lag that would shift the decomposed mean in case of uni-directional averaging. The same technique was applied on the experimental results reported in the previous section.

$$T_{av} = X_{av} * T_{shedding} \quad (6)$$

Applying the resulting moving average on the time history at a sample probe point, the resulting time histories are shown in Fig. 13. As shown in the figure, the total time history plotted contains fluctuation that was decomposed to yield a slowly varying mean. The velocity time history data were collected using a 3 dimensional grid of vertex averaging probes. Adding to the fact that polyhedral cells increase the accuracy due to better approximation of gradients between neighbouring cells, averaging in between vertices adds more confidence to the results monitored by probes.

4.3 Mean component of wind field

A comparison between the CFD and the experimental mean components of the flow for different radial positions is shown in Fig. 14. The plot shows the decomposed mean profiles at a time instant corresponding to the occurrence of the peak mean radial velocity at every location. Comparison between the CFD and the experimental data show that the numerical results follow the development captured by the experimental results. Focusing on the position of maximum velocity ($R=1.0 D_j$), the agreement is more evident, especially for the lower region where the maximum velocities are expected to occur, as well as where most built structures would be. It was expected that, below the roughness height, either shielding or channeling effects would yield misleading results. Therefore, although being one of the key parameters for wind engineering, the height at which the peak velocity occurs was not detected due to it being within the canopy zone of the roughness blocks. Moreover, the plot shown in Fig. 15 illustrates the envelope of radial velocities distribution throughout the entire simulation. The data plotted show that peak radial velocities happen at a radial distance R of $1.0 D_j$, a jet diameter measured from the jet centre. The obtained location matches well with the location of peak wind speed seen in the experiment, as well as the studies conducted by researchers like Kim and Hangan (2007), Sengupta and Sarkar (2008) and Zhang *et al.* (2013). Nevertheless, after close observation, it was found that the streaming effect imposed by the flaps is a contributing factor to the position of peak radial velocity ($R_{max}=1.0 D_j$). This is relatively less than the values found in other studies such as Aboshosha *et al.* (2015b) and Kim and Hangan (2007). Both studies found R_{max} to be in the order of 1.25~1.3. It is believed that simulating a model that follows the same physical conditions as the previous simulations (i.e., no flaps and roughness elements with less significant heights), R_{max} would reach the same values reported by both studies.

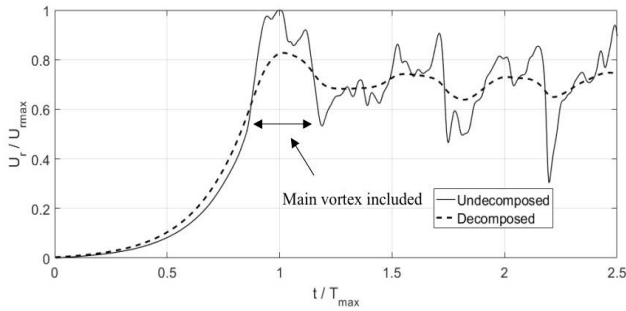


Fig. 13 Decomposed time history at $R/D_j=1$ and $Z/D_j=0.078$

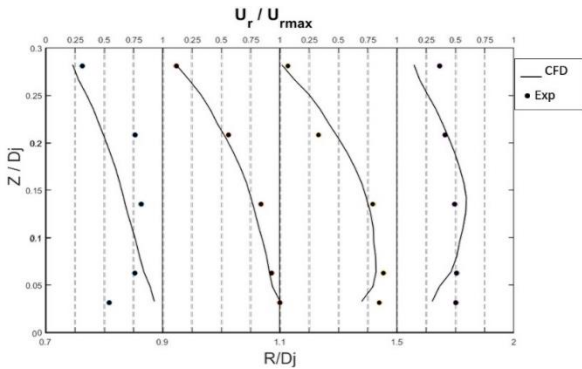


Fig. 14 Mean radial velocity validation

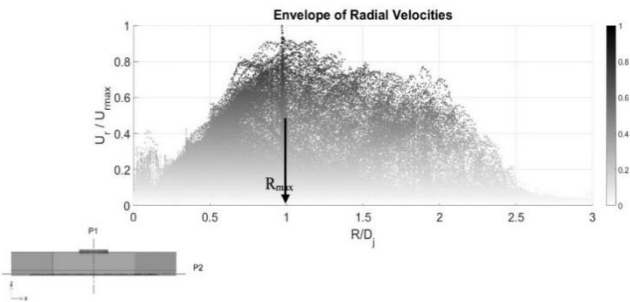


Fig. 15 Envelope of peak radial velocities at P1

4.4 Turbulent component of wind field

4.4.1 Turbulence spectra

Power spectral density of the turbulence resulting from the decomposition technique discussed earlier was generated and plotted in Fig. 16 at the location of the maximum mean (i.e., $R_{max}=1.0 D_j$ and $Z_{max}=0.0625 D_j$) in comparison to that obtained from the experiment for comparison purpose. It is worth noting that although the wind field is nonstationary, it is dealt with as quasi-stationary. This quasi-stationary procedure was applied for the range clipped after 3 Tshedding to avoid the influence of the steady part (post peak) from dominating the analyzed properties. Other studies in the literature dealt with the turbulent component differently to reach a more stationary format before analyzing the turbulent component (Chen and Letchford (2004), Holmes *et al.* (2008), Kwon and Kareem (2009), Lombardo *et al.* (2014) and Zhang *et al.* (2017)). Yet, dealing with the turbulent component as quasi-stationary would provide a simple method of verification by comparing the properties of the LES simulation to that of

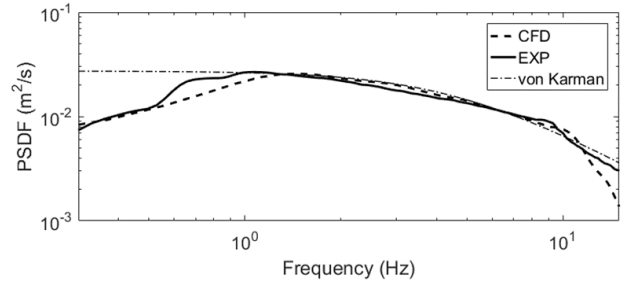


Fig. 16 Power spectral density function validation

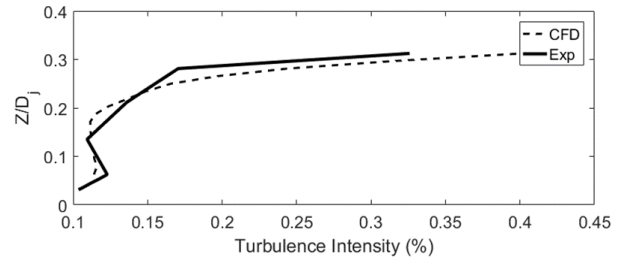


Fig.17 Validation of turbulence intensity profile

the experiment following the same approach. As seen from the figure, PSDFs are in a good agreement, and both collapse on von Karman's empirical model. The match between CFD PSDF and experimental PSDF is up to a certain frequency, which is the maximum frequency of the resolvable eddies by the employed computational mesh. This maximum frequency was found equal to 10 Hz. It can also be noted that the PSDF for downburst speeds collapsed on the fitted von Karman's profile after a frequency of 1.5 Hz (the cut-off frequency) for both experiential and numerical simulations. The fitting procedure using the turbulence length scale as the fitting parameter resulted in a length scale equal to $0.04 D_j$, which is in agreement with the results presented in the last section of this study.

4.4.2 Turbulence intensity

Turbulence intensity I_{ur} represents an important parameter that indicates the relation between the mean and the peak values of turbulent flows. Following Eq. (7), the turbulence intensity is generally defined as the ratio between the statistical root mean square and the mean value of time history. Yet, the fact that the mean component of downburst wind field is not a constant value, requires some adjustment to account for the non-stationarity of downbursts. Accordingly, the statistical properties are calculated within a certain range rather than the complete time history. Following Holmes *et al.* (2008) and Aboshosha *et al.* (2015a), the turbulence intensities were calculated at time instants where the maximum mean velocities occurred. With the time instant known, the clipped range at which statistical properties were computed spreads one-half of the averaging period T_{av} before and after the specified instance. As shown in Eq. (8), the value of the total undecomposed velocity $u(t)$ and the mean velocity corresponding to the considered time step $u(t)$ are used in calculating the standard deviation *orange* of the considered range. The technique was applied on both the

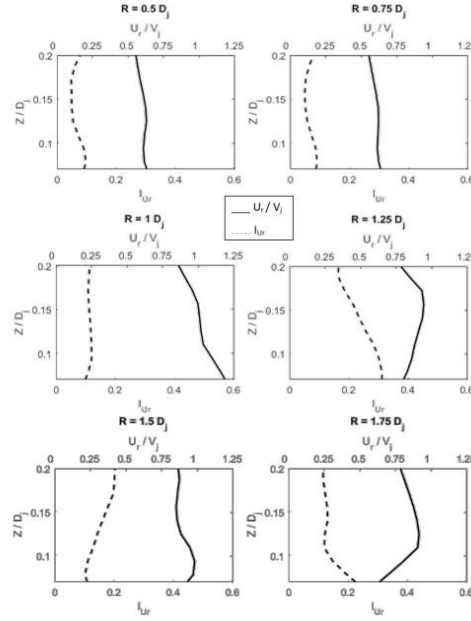


Fig. 18 Turbulence intensity vs mean velocity envelope distribution along height for different radial distances

experimental and the numerical results, and the comparison presented in Fig. 17 for the vertical profile of turbulence intensity at the position of maximum radial velocity shows an excellent agreement between the experimental and the numerical simulations.

$$I_{ur} = \frac{\sigma_{range}}{U_{mean\ range}} \quad (7)$$

$$\sigma_{range} = \sqrt{\frac{\sum(|u(t) - \bar{u}(t)|)^2}{n - 1}} \quad (8)$$

According to the description of the technique elaborated above, the time frame is clear to be a representation of the most important range, that close to the instant of maximum mean. As for the spatial frame, the turbulence intensities were computed for vertical profiles at different radial distances. Aiming to know the variation of I_{ur} along both the vertical and the radial directions, Fig. 18 shows the envelope distribution of I_{ur} along the vertical height at different radial locations. Envelope values are the maximum values at every height, which means that the points forming the profile do not necessarily correspond to the same time instant. It can be noted that the turbulence intensity generally decreases with height for the considered range, which agrees with the results reported by Aboshosha *et al.* (2015a). Moreover, to be able to assess the values plotted, the envelope mean velocities were also plotted for the same considered spatial range. This would provide comparable results to be able to judge the significance of the reported turbulence intensity values. As shown, the turbulence intensities corresponding to the location of maximum mean velocities are about 12%, agreeing with results reported by Holmes *et al.* (2008), Aboshosha *et al.* (2015a) and Zhang *et al.* (2017). It is worth noting that the abrupt increase observed in the turbulence intensity profile at the radial position $R=1.25 D_j$ is believed to be

a result of the formation of the secondary vortex (Kim and Hangan (2007)) causing a sudden change in the wind speed at a rate that is faster than what the averaging filter could eliminate.

4.4.3 Turbulence length scales

Turbulence length scale is a parameter of significant importance as it indicates the average size of eddies in a certain direction at a given position. This type of knowledge is important for applications like dynamic loading of structures where the correlation of turbulence structures might play an impactful role in determining structural response due to this type of loading. Accordingly, the current study computes the length scales in three directions with relevance to the propagation of the flow; radial LR, circumferential L_θ and vertical L_w using procedure similar to that followed by Aboshosha and El Damatty (2015). Calculating all three quantities from time histories of radial velocity, the radial direction was computed by first deducing the time scale τ_{int} as the integration of the autocorrelation function from a time lag of zero, up until the least time lag value at which the autocorrelation function has a zero value. Consequently, Taylor's hypothesis is implemented to deduce the length scale by multiplying the time scale by the corresponding maximum mean velocity at the position at which the time history was probed. Both steps are illustrated by Eqs. (9) and (10).

$$L_R = U_{mean} \times \tau_{int} \quad (9)$$

$$\tau_{int} = \int_{\Delta t=0}^{\tau_{R_\tau(\Delta t)=0}} R_\tau(\Delta t) d\Delta t \quad (10)$$

where L_R is the length scale in the radial direction, U_{mean} is the maximum mean velocity at the probed position, τ_{int} is the time scale, Δt is the time lag and $R_\tau(\Delta t)$ is the

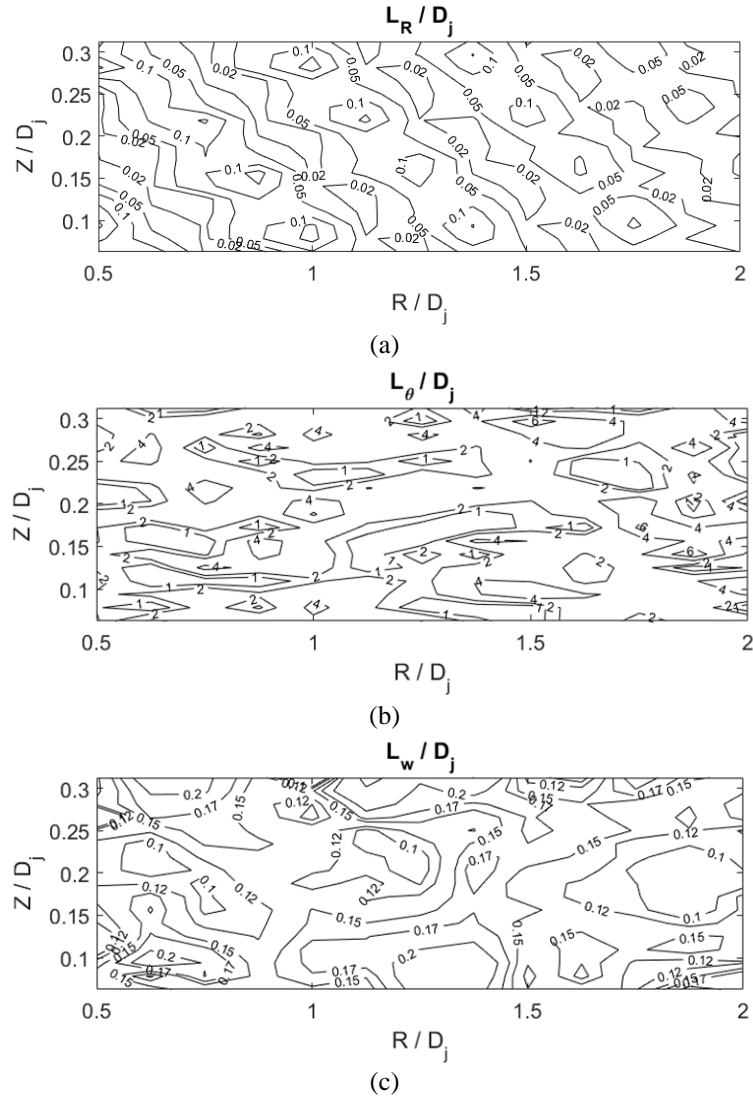


Fig. 19 Spatial distribution of turbulence length scale for (a) radial, (b) circumferential and (c) vertical directions

autocorrelation function.

Alternatively, the length scales in the circumferential and the vertical directions are computed as the fitting parameter of the spatial correlation function, being the correlation between two time histories separated by a given distance in a particular direction. Accordingly, length scales L_θ and L_w for the circumferential and vertical directions respectively are computed by fitting the spatial correlations $R(d\theta)$ and $R(dz)$ using an exponential term as shown in Eqs. (11) and 12.

$$R(d\theta) = \exp\left(-\frac{Rd\theta}{L_\theta}\right) \quad (11)$$

$$R(dz) = \exp\left(-\frac{dz}{L_w}\right) \quad (12)$$

Where $R(d\theta)$ and $R(dz)$ are the spatial correlation functions for the circumferential and vertical directions respectively, R is the radius for the jet centre, $d\theta$ is the angular spatial separation and dz is the vertical spatial separation.

Implementing the procedures mentioned above, the length scales were computed at different radii and heights to demonstrate the spatial variation of the average eddy size in each direction with respect to the jet centre and height from ground level. The contours presented in Fig.19 show the distribution for (a) radial, (b) circumferential and (c) vertical directions. The presented results have been normalized by the jet diameter to give a better perspective on how the results compare to previous literature. Considering the radial direction shown in Fig. 19(a), the presented results show that the length scales in that direction vary from one-tenth of the jet diameter as a maximum, to 20% of that value. The figure also shows a trend that is repeated diagonally. It is believed to be a direct result of the roughness elements used. Given the fact that the elements had a square cross-section of 0.1 m dimension and height of 0.15 m, their presence broke the eddy structures, and is believed to have caused the shown trend. These values are relatively lower than those reported by Aboshosha *et al.* (2015a) who presented values that are at least 5 times those computed by the current study. This is

expected to be a direct result of the grid resolution implemented in the CFD model. With the length scale being an indication of the average eddy size, a coarse grid that would filter eddies with higher frequencies would in turn result in an increase in the average eddy size. This is believed to be the case, where the grid utilized by the authors was relatively coarse, resulting in the exclusion of time scales that would have resulted in lower values for length scales. Nevertheless, the results presented by the current study for L_R provide a better match with the field measurements reported by Zhang *et al.* (2017) who reported an average of 28m for the thunderstorms analyzed in their study. This is despite the fact that the current study performed analysis using the quasi-stationary fluctuating component, while Zhang *et al.* (2017) analyzed a normalized component by dividing it by the time varying standard deviation. Considering an average sized downburst jet diameter (500~1000m), this would translate to (0.03~0.06) L_R / D_j , which matches well with the presented results, especially at radial positions beyond 1.5 times the jet diameter. It is generally expected that the measurements presented by Zhang *et al.* (2017) would mostly be beyond that distance from the jet centre. Moreover, Fig. 19(b) presents the distribution of the circumferential length scale L_θ . The values are relatively large compared to the radial direction, with a dominant value of around 4 times the jet diameter, and a maximum value of 6 times the jet diameter. This confirms the conclusion drawn by Aboshosha *et al.* (2015a) and Holmes *et al.* (2008) that the circumferential direction is very well correlated, which can be critical to horizontally laid out structures such as transmission lines. Yet, the values reported by Aboshosha *et al.* (2015a) were larger than those computed in the current study due to same reason explained for the radial direction, where the grid size used is expected to cause such increase. The same observations were found for the vertical direction, where Fig. 19(c) shows that values of L_w are between one-tenth to one-fifth of the jet diameter for the considered spatial range. This indicates that the correlations are less significant in both the longitudinal and the vertical directions than in the circumferential direction.

5. Conclusions

The current study mainly presented a numerical replication of the downburst simulation done in wind tunnel testing scale in the WindEEE dome for open terrain exposure. The simulation was conducted using an LES with an enhanced grid resolution to capture the flow characteristics through the space and time frames. Afterwards, the analyses results were compared with the experimental results to both validate the CFD results, as well as interpret the flow features shown in the experimental results. Finally, the wind flow characteristics were presented, with special emphasis on the spatial distribution of turbulence characteristics. The following points summarize the findings of results comparison:

- The comparison of mean wind speeds showed good agreement between the experiment and the CFD

simulation.

- Results showed maximum radial speed occurring at a radial distance equal to the jet diameter, noticeably less than values in the literature. This was found to be attributed to the inlet flaps cross-section, as well as the roughness elements used.
- Examining the wind field development showed the flaps had a streaming effect on the flow. It was shown that the effect was manifested through the streaming imposed on the descending downdraft. The roughness blocks were also shown to canopy the region within their height, as well as entrap the inner portion of the downdraft column.
- Comparisons of the non-spatial turbulence characteristics (PSDF and turbulence intensity) showed a good agreement between the CFD model and experimental results.
- Turbulence intensity profiles were presented against the envelope mean radial velocity profiles. Results showed turbulence intensity is about 12% at the peak velocity position, agreeing with previous literature.
- Length scales in three directions were presented, and were found to be in the order of 0.1, 4 and 0.2 times the jet diameter for the radial, circumferential and vertical directions respectively. Values were compared to those reported in the literature, and seemed to give a justifiable match.

Most importantly, the current study provides a validated CFD model that replicated a wind tunnel scale experiment and yielded acceptable results. This can be used to model simulations of higher complexity, in full scale, to explore finer details of the downburst wind field which can be of great aid when assessing the effect of such hazards on structural applications

Acknowledgments

The authors would like gratefully acknowledge the financial support of Hydro One Inc., the National Research Council of Canada (NSERC) as well as the Ontario Centres of Excellence (OCE). The authors are also acknowledging the technical collaboration and advice provided by the WindEEE Research Institute knowledgeable staff. Also, the authors are grateful to Dr. Amal Elawady at FIU for sharing and explaining the experimental wind-field data. Lastly, the computational work could not be realized without the resources and technical support of SHARCNET high performance computing platform.

References

- Aboshosha, H. and El Damatty, A. (2015), "Engineering method for estimating the reactions of transmission line conductors under downburst winds", *Eng. Struct.*, **99**, 272-284. <https://doi.org/10.1016/j.engstruct.2015.04.010>.
- Aboshosha, H., Bitsuamlak, G. and El Damatty, A. (2015a), "Turbulence characterization of downbursts using LES", *J. Wind Eng. Ind. Aerod.*, **136**, 44-61. <https://doi.org/10.1016/j.jweia.2014.10.020>.

- Aboshosha, H., Elawady, A., El Ansary, A. and El Damatty, A. (2016), "Review on dynamic and quasi-static buffeting response of transmission lines under synoptic and non-synoptic winds", *Eng. Struct.*, **112**(1), 23-46. <https://doi.org/10.1016/j.engstruct.2016.01.003>.
- Aboshosha, H., Elshaer, A., Bitsuamlak, G.T. and El Damatty, A. (2015b), "Consistent inflow turbulence generator for LES evaluation of wind-induced responses for tall buildings", *J. Wind Eng. Ind. Aerod.*, **142**, 198-216. <https://doi.org/10.1016/j.jweia.2015.04.004>.
- ANSYS Inc. (2016), ANSYS® FLUENT, Release 17.0, Theory Guide.
- Chay, M.T. and Letchford, C.W. (2002), "Pressure distributions on a cube in a simulated thunderstorm downburst. Part B: moving downburst observations", *J. Wind Eng. Ind. Aerod.*, **90**(7), 733-753. [https://doi.org/10.1016/S0167-6105\(02\)00163-0](https://doi.org/10.1016/S0167-6105(02)00163-0).
- Chay, M.T., Albermani, F. and Wilson, R. (2006), "Numerical and analytical simulation of downburst wind loads", *Eng. Struct.*, **28**(2), 240-254. <https://doi.org/10.1016/j.engstruct.2005.07.007>.
- Chen, L. and Letchford, C.W. (2004), "A deterministic-stochastic hybrid model of downbursts and its impact on a cantilevered structure", *Eng. Struct.*, **26**(5), 619-629. <https://doi.org/10.1016/j.engstruct.2003.12.009>.
- Choi, E.C.C. (2004), "Field measurement and experimental study of wind speed profile during thunderstorms", *J. Wind Eng. Ind. Aerod.*, **92**(3-4), 275-290. <https://doi.org/10.1016/j.jweia.2003.12.001>.
- Das, K.K., Ghosh, A.K. and Sinhamahapatra, K.P. (2011), "Physical simulation of dry microburst using impinging jet model with swirl", *Int. J. Eng. Sci. Technol.*, **3**(5), 20-29.
- Dempsey, D. and White, H.B. (1996), "Winds wreak havoc on lines", *Transm. Distrib. World*, **48**(6), 32-42.
- Elawady, A., Aboshosha, H., El Damatty, A., Bitsuamlak, G., Hangan, H. and Elatar, A. (2017), "Aero-elastic testing of multi-spanned transmission line subjected to downbursts", *J. Wind Eng. Ind. Aerod.*, **169**, 194-216. <https://doi.org/10.1016/j.jweia.2017.07.010>.
- Elawady, A., Aboshosha, H., El Damatty, A.A. and Bitsuamlak, G. (2016), "Wind tunnel testing of a multiple span aeroelastic transmission line subjected to downburst wind in resilient infrastructure", *CSCE 2016*, ID538.
- Elawady, A., El Damatty, A.A. (2016), "Longitudinal force on transmission towers due to non-symmetric downburst conductor loads", *Eng. Struct.*, **127**(15), 206-226. <https://doi.org/10.1016/j.engstruct.2016.08.030>.
- Elshaer, A., Aboshosha, H., Bitsuamlak, G., El Damatty, A.A. and Dagnew, A. (2016), "LES evaluation of wind-induced responses for an isolated and a surrounded tall building", *Eng. Struct.*, **115**, 179-195. <https://doi.org/10.1016/j.engstruct.2016.02.026>.
- Germano, M., Piomelli, U., Moin, P. and Cabot, W.H. (1991), "A dynamic subgrid-scale eddy viscosity model", *Phys. Fluids*, **3**, 1760. <https://doi.org/10.1063/1.857955>.
- Gunter, W.S. and Schroeder, J.L. (2015), "High-resolution full-scale measurements of thunderstorm outflow winds", *J. Wind Eng. Ind. Aerod.*, **138**, 13-26. <https://doi.org/10.1016/j.jweia.2014.12.005>.
- Hadziabdić, M. (2005), "LES, RANS and Combined Simulation of Impinging Flows and Heat Transfer. Simulation", Ph.D. Dissertation, Technical University of Delft. The Netherlands.
- Hjelmfelt, M.R. (1988), "Structure and life cycle of microburst outflows observed in Colorado", *J. Appl. Meteorol.*, **27**(8), 900-927. [https://doi.org/10.1175/1520-0450\(1988\)027%3C0900:SALCOM%3E2.0.CO;2](https://doi.org/10.1175/1520-0450(1988)027%3C0900:SALCOM%3E2.0.CO;2).
- Holmes, J.D., Hangan, H.M., Schroeder, J.L., Letchford, C.W. and Orwig, K.D. (2008), "A forensic study of the Lubbock-Reese downdraft of 2002", *Wind Struct.*, **11**(2), 137-152. <https://doi.org/10.12989/was.2008.11.2.137>.
- Kim, J. and Hangan, H. (2007), "Numerical simulations of impinging jets with application to downbursts", *J. Wind Eng. Ind. Aerod.*, **95**(4), 279-298. <https://doi.org/10.1016/j.jweia.2006.07.002>.
- Kwon, D.K. and Kareem, A. (2009), "Gust-front factor: new framework for wind load effects on structures", *J. Struct. Eng.*, **135**(6), 717-732. [https://doi.org/10.1061/\(ASCE\)0733-9445\(2009\)135:6\(717\)](https://doi.org/10.1061/(ASCE)0733-9445(2009)135:6(717)).
- Li, C.Q. (2000), "A stochastic model of severe thunderstorms for transmission line design", *Probabilistic Eng. Mech.*, **15**(4), 359-364. [https://doi.org/10.1016/S0266-8920\(99\)00037-5](https://doi.org/10.1016/S0266-8920(99)00037-5).
- Li, H. and Ou, J. (2012), "Experimental simulation of downburst-generated wind loading on building structure", *The Seventh International Colloquium on Bluff Body Aerodynamics and Applications*, Shanghai, China.
- Lilly, D.K. (1992), "A proposed modification of the Germano subgrid-scale closure method", *Phys. Fluids*, **4**(3) 633-635. <https://doi.org/10.1063/1.858280>.
- Lin, W.E., Orf, L., Savory, E. and Novacco, C. (2007), "Proposed large-scale modelling of the transient features of a downburst outflow", *Wind Struct.*, **10**(4), 315-346.
- Lombardo, F.T., Smith, D.A., Schroeder, J.L. and Mehta, K.C. (2014), "Thunderstorm characteristics of importance to wind engineering", *J. Wind Eng. Ind. Aerod.*, **125**, 121-132. <https://doi.org/10.1016/j.jweia.2013.12.004>.
- Mason, M.S., Fletcher, D.F. and Wood, G.S. (2010), "Numerical simulation of idealised three-dimensional downburst wind fields", *Eng. Struct.*, **32**(11), 3558-3570. <https://doi.org/10.1016/j.engstruct.2010.07.024>.
- Mason, M.S., Letchford, C.W. and James, D.L. (2005), "Pulsed wall jet simulation of a stationary thunderstorm downburst, Part A: Physical structure and flow field characterization", *J. Wind Eng. Ind. Aerod.*, **93**(7), 557-580. <https://doi.org/10.1016/j.jweia.2005.05.006>.
- Mason, M.S., Wood, G.S. and Fletcher, D.F. (2009), "Numerical simulation of downburst winds", *J. Wind Eng. Ind. Aerod.*, **97**(11-12), 523-539. <https://doi.org/10.1016/j.jweia.2009.07.010>.
- McConville, A.C., Sterling, M. and Baker, C.J. (2009), "The physical simulation of thunderstorm downbursts using an impinging jet", *Wind Struct.*, **12**(2), 133-139. <http://doi:10.12989/was.2009.12.2.133>.
- Orwig, K.D. and Schroeder, J.L. (2007), "Near-surface wind characteristics of extreme thunderstorm outflows", *J. Wind Eng. Ind. Aerod.*, **95**(7), 565-584. <https://doi.org/10.1016/j.jweia.2006.12.002>.
- Otsuka, K. (2006), "Effects of topography on the surface wind of an isolated wet microburst", *The Fourth International Symposium on Computational Wind Engineering*. Yokohama, Japan.
- Sengupta, A. and Sarkar, P.P. (2008), "Experimental measurement and numerical simulation of an impinging jet with application to thunderstorm microburst winds", *J. Wind Eng. Ind. Aerod.*, **96**(3), 345-365. <https://doi.org/10.1016/j.jweia.2007.09.001>.
- Sengupta, A., Haan, F.L., Sarkar, P.P. and Balamurdu, V. (2008), "Transient loads on buildings in microburst and tornado winds", *J. Wind Eng. Ind. Aerod.*, **96**(10-11), 2173-2187. <https://doi.org/10.1016/j.jweia.2008.02.050>.
- Solari, G., Burlando, M., Gaetano, P. De and Repetto, M.P. (2015a), "Characteristics of thunderstorms relevant to the wind loading of structures", *Wind Struct.*, **20**(6), 763-791. <http://dx.doi.org/10.12989/was.2015.20.6.763>.
- Solari, G., De Gaetano, P. and Repetto, M.P. (2015b), "Thunderstorm response spectrum: fundamentals and case study", *J. Wind Eng. Ind. Aerod.*, **143**, 62-77. <https://doi.org/10.1016/j.jweia.2015.04.009>.
- Tamura, Y. and Kareem, A. (2013), "Advanced Structural Wind Engineering", Springer, Berlin, Germany.

- Theodore Fujita, T. (1985), "The downburst: microburst and macroburst", *Report of Projects NIMROD and JAWS*, University of Chicago. Chicago. U.S.A.
- Vermeire, B.C., Orf, L.G. and Savory, E. (2011), "Improved modelling of downburst outflows for wind engineering applications using a cooling source approach", *J. Wind Eng. Ind. Aerod.*, **99**(8), 801-814. <https://doi.org/10.1016/j.jweia.2011.03.003>.
- Wolfson, M.M., DiStefano, J.T. and Fujita, T.T. (1985), "Low altitude wind shear in the Memphis, TN area based on Mesonet and LLWAS data", *In Preprints, 14th Conf. on Severe Local Storms, Indianapolis, IN, Amer. Meteor. Soc.*
- Wood, G.S., Kwok, K.C.S., Motteram, N.A. and Fletcher, D.F. (2001), "Physical and numerical modelling of thunderstorm downbursts", *J. Wind Eng. Ind. Aerod.*, **89**(6), 535-552. [https://doi.org/10.1016/S0167-6105\(00\)00090-8](https://doi.org/10.1016/S0167-6105(00)00090-8).
- Xu, Z. and Hangan, H. (2008), "Scale, boundary and inlet condition effects on impinging jets", *J. Wind Eng. Ind. Aerod.*, **96**(12), 2383-2402. <https://doi.org/10.1016/j.jweia.2008.04.002>.
- Zhang, S., Solari, G., De Gaetano, P., Burlando, M. and Repetto, M.P. (2017), "A refined analysis of thunderstorm outflow characteristics relevant to the wind loading of structures", *Probabilistic Eng. Mech.*, **54**, 9-24. <https://doi.org/10.1016/j.probengmech.2017.06.003>.
- Zhang, Y., Hu, H. and Sarkar, P.P. (2013), "Modeling of microburst outflows using impinging jet and cooling source approaches and their comparison", *Eng. Struct.*, **56**, 779-793. <https://doi.org/10.1016/j.engstruct.2013.06.003>.